Eddy-driven nutrient transport and associated upper-ocean primary production along the Kuroshio

Uchiyama, Yusuke
Suzue, Yota
Yamazaki, Hidekatsu

(Citation)
Journal of Geophysical Research: Oceans,122(6):5046-5062

(Issue Date)
2017-06

(Resource Type)
journal article

(Version)
Version of Record

AGU PUBLICATIONS

JGR

Journal of Geophysical Research: Oceans

RESEARCH ARTICLE

10.1002/2017JC012847

Key Points:

- The primary production along the Kuroshio is examined using a climatological, high-resolution, coupled circulation-biogeochemical model
- Eddy-driven downward nitrate transport suppresses the primary production in the Kuroshio Region by shear and baroclinic instabilities
- In turn, the downwelling is much less pronounced in the Kuroshio Extension, where nitrate upwelling due to cyclonic eddies prevails

Correspondence to:
Y. Uchiyama,
uchiyama@harbor.kobe-u.ac.jp

Citation:
Uchiyama, Y., Y. Suzue, and H. Yamazaki (2017), Eddy-driven nutrient transport and associated upper-ocean primary production along the Kuroshio, *J. Geophys. Res. Oceans*, *122*, 5046–5062, doi:10.1002/2017JC012847.

Received 28 FEB 2017
Accepted 23 MAY 2017

Eddy-driven nutrient transport and associated upper-ocean primary production along the Kuroshio

Yusuke Uchiyama[1,2,3], Yota Suzue[1], and Hidekatsu Yamazaki[3,4]

[1]Department of Civil Engineering, Kobe University, Kobe, Japan, [2]Coastal and Estuarine Environment Division, Port and Airport Research Institute, Yokosuka, Japan, [3]Core Research for Evolutionary Science and Technology, Japan Science and Technology Agency, Tokyo, Japan, [4]Department of Ocean Sciences, Tokyo University of Marine Science and Technology, Tokyo, Japan

Abstract The Kuroshio is one of the most energetic western boundary currents accompanied by vigorous eddy activity both on mesoscale and submesoscale, which affects biogeochemical processes in the upper ocean. We examine the primary production around the Kuroshio off Japan using a climatological ocean modeling based on the Regional Oceanic Modeling System (ROMS) coupled with a nitrogen-based nutrient, phytoplankton and zooplankton, and detritus (NPZD) biogeochemical model in a submesoscale eddy-permitting configuration. The model indicates significant differences of the biogeochemical responses to eddy activities in the Kuroshio Region (KR) and Kuroshio Extension Region (KE). In the KR, persisting cyclonic eddies developed between the Kuroshio and coastline are responsible for upwelling-induced eutrophication. However, the eddy-induced vertical nutrient flux counteracts and promotes pronounced southward and downward diapycnal nutrient transport from the mixed-layer down beneath the main body of the Kuroshio, which suppresses the near-surface productivity. In contrast, the KE has a 23.5% higher productivity than the KR, even at comparable eddy intensity. Upward nutrient transport prevails near the surface due to predominant cyclonic eddies, particularly to the north of the KE, where the downward transport barely occurs, except at depths deeper than 400 m and to a much smaller degree than in the KR. The eddy energy conversion analysis reveals that the combination of shear instability around the mainstream of the Kuroshio with prominent baroclinic instability near the Kuroshio front is essential for the generation of eddies in the KR, leading to the increase of the eddy-induced vertical nitrate transport around the Kuroshio.

1. Introduction

The marine ecosystem acts to mediate global warming by absorbing and fixing carbon in the ocean. *Nellemann et al.* [2009] reported that marine organisms account for more than 50% of all biological carbon in the world. The estimated carbon fixation due to primary production in the coastal seas is approximately 250 g m^{-2} yr^{-1}, which is approximately twice as much as that in the open ocean [*Martin et al.*, 1987]. At the coastal margins, active primary production mainly occurs due to the nutrient supply to the upper ocean through terrestrial and riverine discharge and coastal upwelling, whereas the productivity in the open ocean is generally much smaller than that in coastal regions. Nevertheless, the open ocean occupies approximately 90% of the ocean, substantially influencing the global carbon cycle and its inventory. Eddies and other mesoscale processes, such as fronts and filaments, are ubiquitous in the upper ocean, potentially affecting the biological production. Because nutrients are transported vertically from the nutrient-rich subsurface to the euphotic zone by localized upwelling due to cyclonic mesoscale eddies and fronts, the high-productivity manifests mostly around them in the open ocean [e.g., *Falkowski et al.*, 1991; *Strass*, 1992]. Satellite ocean color images revealed that the spatial variability in the surface chlorophyll is distributed not only on the mesoscale [e.g., *Gower et al.*, 1980] but also on the submesoscale [e.g., *Denman and Abbott*, 1994]. Numerical studies have been conducted in idealized configurations to examine the influences of the mesoscale and submesoscale variability on the biological production [e.g., *Franks and Walstad*, 1997; *Spall and Richards*, 2000; *Lévy et al.*, 2001; *Lévy*, 2003; *Pasquero*, 2005; *Bracco et al.*, 2009]. In addition, regional biological responses to the mesoscale and submesoscale variability have been observed in the northern Gulf of Alaska [e.g., *Crawford et al.*, 2007] and were modeled in synoptic regional configurations for the North Atlantic [e.g., *Oschlies and Garçon*, 1998; *Oschlies*, 2002], yet explicitly focusing on the enhancement of

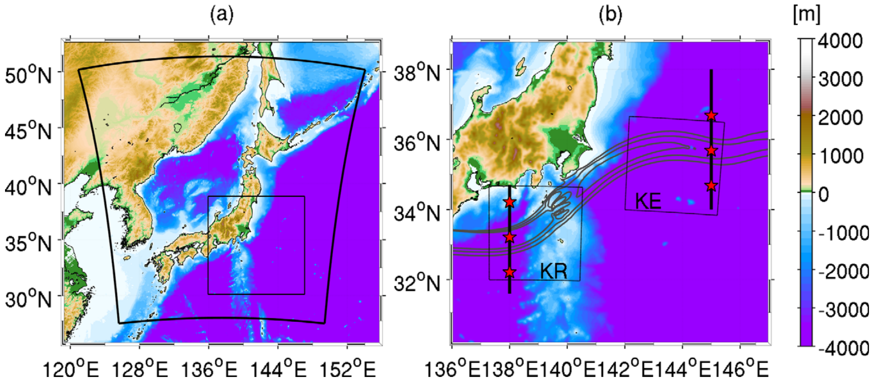

Figure 1. (a) The ROMS-NPZD model domain (bold box) and bathymetry (color: m); and (b) blow-up region shown by the thin box in (a) with the surface velocity magnitude greater than 0.5 m s^{-1} at intervals of 0.25 m s^{-1} (gray contours). Also shown in Figure 1b as black thin rectangles are the approximate extents of the Kuroshio Region (KR) and the Kuroshio Extension Region (KE) used for the kinetic energy spectra in Figure 4, the two transects at 138°E and 145°E (black lines) used for the cross-sectional plots in Figures 10, 12, 14, and 15, and for Table 3. The red star marks the locations for the Hovmöller plots in Figures 7 and 8.

primary production associated with eddy-induced upwelling. However, recent studies have suggested that eddies could conversely suppress the productivity. For instance, *Gruber et al.* [2011] showed that unusual low productivity might be caused by eddy-induced downward nutrient transport in eastern boundary upwelling systems including the U.S. West Coast, where an abundant supply of upward transport of subsurface nutrients is generally expected.

The Kuroshio is the energetic western boundary current of the North Pacific Subtropical Gyre. It flows northeastward along the continental shelf break on the Pacific side of Japan and then detaches off the Boso Peninsula at ~35.6°N and 141.0°E, followed by further eastward veering to enter the North Pacific as a free jet referred to as the Kuroshio Extension (Figure 1). The Kuroshio off Japan is accompanied by vigorous eddy and frontal activity both on the mesoscale and submesoscale [cf., *Waseda et al.*, 2003]. Observations have shown that cyclonic eddies associated with the Kuroshio enhance the chlorophyll-a (chl-a) concentration to ~2.5 μg L^{-1} and the associated carbon production rate of 40 g C m^{-2} [e.g., *Kimura et al.*, 1997; *Nakata et al.*, 2000] in the Enshunada Sea, which we call the "Kuroshio Region (KR)" (Figure 1b, left box). Note that in the present study, we assume that chl-a is used as a proxy of the primary production [e.g., *Behrenfeld and Falkowski*, 1997; *Tiera et al.*, 2005]. In contrast, in the Kuroshio Extension Region (KE; right box in Figure 1b), both the upward and downward nutrient transport have been observed near the Kuroshio front [*Clayton et al.*, 2014], resulting from concurrent adiabatic isopycnal subduction and diabatic diapycnal turbulent mixing [*Nagai et al.*, 2012]. Such a subduction was also detected for the Kuroshio front in the East China Sea as downward transport of the less saline surface water [*Matsuno et al.*, 2009] in which ageostrophic cross-frontal flow due to baroclinic instability [e.g., *Spall*, 1995] crucially interplayed with the shallow shelf-break topography. However, *Sasai et al.* [2007, 2010] demonstrated that cyclonic eddies promote the primary productivity in the KE based on the MOM3-based OFES model [*Masumoto et al.*, 2004] in a mesoscale eddy-resolving configuration coupled with the nitrogen-based NPZD model of *Oschlies* [2001]. Therefore, whether oceanic eddies in the upper ocean along the Kuroshio promote localized upwelling-induced eutrophic conditions or subduction/downwelling-induced oligotropic conditions are a quite fundamental but open question.

In the present study, we conduct a high-resolution, mesoscale eddy-resolving, submesoscale eddy-permitting simulation around Japan encompassing an extensive portion of the Kuroshio in a climatological setting for ten years with a horizontal resolution of 3 km. The model is based on the Regional Oceanic Modeling System (ROMS) [cf., *Shchepetkin and McWilliams*, 2005, 2008] coupled with a simplified version of the nitrogen-based pelagic NPZD biogeochemical model of *Fasham et al.* [1990], *Moisan and Hofmann* [1996], and *Di Lorenzo et al.* [2004], embedded in and initialized by the Japan Coastal Ocean Prediction Experiment 2 (JCOPE2) assimilative oceanic reanalysis [*Miyazawa et al.*, 2009] with the atmospheric forcing from the Grid Point Value of the Global Spectral Model (GPV-GSM) assimilative atmospheric product [e.g., *Roads*, 2004]. We aim to clarify the biogeochemical responses to mesoscale and submesoscale oceanic variability through eddy-induced nutrient transport. Particular attention is paid to substantial differences in the primary production and its driving mechanism in the KR and KE regions. The remainder of this paper is organized as follows. A description of the coupled climatological model configuration is presented in section 2. Section 3 describes the model-data comparisons to validate the model with respect to the mean dynamics, eddy activities, and surface biological production around the Kuroshio. Subsequently, analyses and discussions on the eddy-induced nitrate transport (section 4) and its driving mechanism based on eddy energy conversion analysis (section 5) are provided, followed by conclusions in section 6.

2. Methods

2.1. Hydrodynamic Model

The downscaling oceanic modeling for the Kuroshio region off Japan (Figure 1) is based on a research version of ROMS developed privately at University of California, Los Angeles (A. F. Shchepetkin, personal communication). The ROMS model is a terrain-following, hydrostatic regional ocean circulation model expressed in horizontal curvilinear coordinate and vertically stretched surface-following and terrain-following *s* coordinate [*Shchepetkin and McWilliams*, 2005]. The K-Profile Parameterization (KPP) mixed-layer turbulence model [*Large et al*., 1994] is employed for the vertical momentum and tracer mixing, while the lateral mixing is not explicitly taken into account other than biharmonic hyperdiffusion inherent in the third order upstream-biased lateral advection scheme. The monthly climatology of the JCOPE2 reanalysis [*Miyazawa et al*., 2009] is exploited to initialize the ROMS model, and to impose open boundary conditions of sea surface height (SSH), temperature, salinity, and zonal and meridional horizontal current velocities. The JCOPE2 is the operational oceanic reanalysis product for the northwestern Pacific with a horizontal resolution of ~10 km incorporating 3-D-VAR data assimilation with a vast amount of satellite and in situ observations such as the Argo profiling floats. We rely on the one-way offline nesting approach described in *Mason et al*. [2010] to convey the basin-scale information in the parent JCOPE2 into the child ROMS model. The ROMS model is designed to encompass the KR and KE regions around Japan, consisting of 784 × 864 horizontal grid cells with 3 km horizontal resolution and 32 vertically stretched terrain-following and surface-following *s*-layers. The model topography is obtained from the SRTM30_PLUS product [*Rodriguez et al*., 2005; *Becker et al*., 2009], which covers the global ocean at 30 geographic arc seconds, supplemented by the J-EGG500 (http://www.jodc.go.jp/data_set/jodc/jegg_intro.html) at 500 m resolution for the coastal region around Japan. Surface wind stresses are imposed from the daily climatology of the GPV-GSM operational atmospheric product of the Japan Meteorological Agency (JMA) at the resolution of TL959L60 (viz., at ~20 km horizontally). Surface heat, freshwater, and radiation fluxes are based on the NOAA-COADS monthly climatology [*Woodruff et al*., 1987]. To improve the reproducibility of the Kuroshio, we introduce a four-dimensional nudging (also known as robust diagnostic) [e.g., *Marchesiello et al*., 2003] for temperature and salinity (TS) with a weak nudging inverse time scale of 1/20 d^{-1} toward the 10 day averaged climatological JCOPE2 TS fields. The numerical configuration is summarized in Table 1.

2.2. Biogeochemical Model

The biogeochemical model is based on a nitrogen-based NPZD pelagic model [*Fasham et al*., 1990; *Moisan and Hofmann*, 1996; and *Di Lorenzo et al*., 2004], and the numerical configuration follows that of *Gruber et al*. [2006]. The present NPZD model is reconciled for examining the biological responses to the ambient hydrodynamics as simple as possible, and, thus, is reduced to consider the concentrations (mmol Nm^{-3}) of only five components: nitrate $[NO_3^-]$, ammonium $[NH_4^+]$, phytoplankton $[Phyt]$, zooplankton $[Zoo]$, and detritus $[Det]$. The full set of conservation equations with the source and sink terms for each of the five components is written as:

Table 1. Numerical Configurations

Computational period	10 years (climatological run)
Grid cells	784 × 864 (× 32 vertical *s*-layers)
Horizontal grid resolution	3 km
Baroclinic time step	150 s
Surface wind stress	JMA GPV-GSM (daily climatology)
Surface flux	NOAA COADS (monthly climatology)
SST to restore	Pathfinder-AVHRR (monthly climatology)
Initial/boundary conditions	JCOPE2 (monthly climatology)
TS nudging	JCOPE2 (10 day averaged)
Topography	SRTM30_Plus supplemented by J-EGG500

$$\frac{D}{Dt}\left[NO_3^-\right] = -Q_1, \qquad (1)$$

$$\frac{D}{Dt}\left[\mathrm{NH}_4^+\right]=-Q_2+\mu_{[Zoo]\left[\mathrm{NH}_4^+\right]}\cdot[Zoo]+\mu_{[Det]\left[\mathrm{NH}_4^+\right]}\cdot[Det], \tag{2}$$

$$\frac{D}{Dt}[Phyt]=-\left(\mu_{[Phyt]}+\mu_{[Phyt][Det]}\right)\cdot[Phyt]-G+Q_1+Q_2, \tag{3}$$

$$\frac{D}{Dt}[Zoo]=-\left(\mu_{[Zoo]}+\mu_{[Zoo]\left[\mathrm{NH}_4^+\right]}+\mu_{[Zoo][Det]}\right)\cdot[Zoo]+\beta\cdot G, \tag{4}$$

$$\frac{D}{Dt}[Det]=-\left(\mu_{[Det]}+\mu_{[Det]\left[\mathrm{NH}_4^+\right]}\right)\cdot[Det]+(1-\beta)\cdot G+\mu_{[Phyt][Det]}\cdot[Phyt], \tag{5}$$

where D/Dt is the material derivative including the tendency, 3-D advection, vertical settling of $[Phyt]$, $[Zoo]$, and $[Det]$, and vertical eddy diffusive fluxes determined by the KPP model. Similarly to the hydrodynamic model ROMS, the horizontal subgrid scale diffusion is not explicitly introduced in the NPZD model. The rate of nitrate uptake by phytoplankton (Q_1), the rate of ammonium uptake by phytoplankton (Q_2), and the rate of phytoplankton grazing by zooplankton (G) are given by:

$$Q_1=\frac{\alpha_J\cdot[Phyt]\cdot\left[\mathrm{NO}_3^-\right]\cdot e^{-\varnothing\cdot\left[\mathrm{NH}_4^+\right]}}{K_{\mathrm{NO}_3^-}+\left[\mathrm{NO}_3^-\right]}, \tag{6}$$

$$Q_2=\frac{\alpha_J\cdot[Phyt]\cdot\left[\mathrm{NH}_4^+\right]}{K_{NH_4^+}+\left[\mathrm{NH}_4^+\right]}, \tag{7}$$

$$G=\frac{g_{\max}\cdot[Phyt]\cdot[Zoo]}{K_{Phyt}+[Phyt]}\quad. \tag{8}$$

where α_J is the light limited growth rate in d^{-1} as a function of photosynthetically active radiation (PAR) and the maximum growth rate [*Fasham et al.*, 1990, equations (4) and (5)]. Chlorophyll-a concentration is retrieved by equation (8) in *Gruber et al.* [2006]. The other model parameters are modestly tuned for the study site as summarized in Table 2.

The initial and boundary conditions for nitrate and phytoplankton are obtained from the World Ocean Atlas 2005 (WOA05) [e.g., *Garcia et al.*, 2006] and the MODIS/Aqua satellite data (https://oceancolor.gsfc.nasa.gov/cms/data/aqua). The nitrate concentration is imposed as a combination of the seasonal (for depths down to 500 m) and annual (below 500 m depth) climatology. Because the resolution of the WOA05 is 1° × 1°, which is too coarse to correctly represent the coastal nitrate, the initial concentration near the coast shallower than 500 m is linearly interpolated in the vertical toward the vertical nitrate profiles at 500 m depth. Vertical profiles of phytoplankton concentration are inferred from the monthly climatology of the surface chlorophyll-a (chl-a) from the MODIS/Aqua using the algorithm proposed by *Morel and Berthon* [1989] for the initial and open boundary conditions. The zooplankton concentration is assumed to be proportional to chl-a [*Gruber et al.*, 2006]. The remaining variables, ammonium and detritus, are set to zero in the initial and boundary conditions. Note that all the reanalysis, satellite, and in situ data used in the present study are publically available. The coupled ROMS-NPZD model is run for ten years in a climatological configuration.

Table 2. Parameters of the Biogeochemical Model

Parameter	Symbol	Value	Unit
Half-saturation for phytoplankton NO_3^- uptake	$K_{\mathrm{NO}_3^-}$	1.5	mmol N m^{-3}
Half-saturation for phytoplankton NH_4^+ uptake	$K_{\mathrm{NH}_4^+}$	0.5	mmol N m^{-3}
Phytoplankton ammonium inhibition parameter	$\varnothing$	1.5	$(\mathrm{mmol\ N})^{-1}$
Phytoplankton loss to sink rate	$\mu_{[Phyt]}$	0.01	d^{-1}
Phytoplankton mortality to detritus rate	$\mu_{[Phyt][Det]}$	0.072	d^{-1}
Zooplankton maximum growth rate	$g_{\max}$	0.75	d^{-1}
Zooplankton assimilation efficiency	β	0.75	n.d.
Zooplankton half-saturation for ingestion	K_{Phyt}	1.0	d^{-1}
Zooplankton loss to sink	$\mu_{[Zoo]}$	0.025	d^{-1}
Zooplankton specific excretion rate	$\mu_{[Zoo]\left[\mathrm{NH}_4^+\right]}$	0.1	d^{-1}
Zooplankton mortality to detritus	$\mu_{[Zoo][Det]}$	0.025	d^{-1}
Detrital loss to sink rate	$\mu_{[Det]}$	0.02	d^{-1}
Detrital breakdown to NH_4^+ rate	$\mu_{[Det]\left[\mathrm{NH}_4^+\right]}$	0.03	d^{-1}

The results for the 10th model year are utilized in the following analyses unless otherwise stated. Initial adjustments during the model spin-up occurred mostly in the first model year, while approximately periodic, climatological results are obtained after the third model year.

3. Upper-Ocean Dynamics and Biogeochemistry

3.1. Upper-Ocean Dynamics

First of all, the model results are compared for validation with the delayed-time AVISO satellite altimetry data (viz., gridded daily SSH composite at 1/4° resolution) [e.g., *Traon et al*., 1998], Merged satellite and in situ data Global Daily Sea Surface Temperature (MGDSST, at 1/4° resolution) [*Sakurai et al*., 2005], and the JCOPE2 reanalysis (Figure 2). The annual mean climatology is obtained from 20 year averages (1994–2013) of each of the three data sets. The Kuroshio main body visualized by the time-averaged near-surface geostrophic current velocity estimated from the AVISO-SSH is approximately the same as that of the JCOPE2 and ROMS models (Figures 2a–2c). Although ROMS yields slightly faster velocities due to the grid-size refinement from 10 km (JCOPE2) to 3 km (ROMS), which allows to more realistically resolve the buoyancy gradient and results in the geostrophic acceleration of the Kuroshio, the overall pattern resembles that of the AVISO and JCOPE2. Likewise, the model-derived SST shows a satisfactory agreement with the MGDSST and JCOPE2, particularly the sharp transition along the Kuroshio fronts (Figures 2d–2f). A modest deficiency in the SST reproducibility is found in ROMS, which is most conceivable in the northern part of the Japan Sea, whereas this warm bias is already inherent in the parent JCOPE2. Hence, we conclude that the present JCOPE2-ROMS downscaling model is sufficiently capable of reproducing the mean oceanic hydrodynamics along the Kuroshio off Japan.

3.2. Eddy Activity Near the Surface

Figure 3 shows the daily averaged relative vorticity near the surface normalized by the background rotation *f* (the Coriolis parameter) in winter (1 January) and summer (1 August) in the tenth model year. Horizontal velocity shear associated with the Kuroshio generates axisymmetric pairs of positive (viz., counterclockwise rotating, cyclonic) and negative (viz., clockwise rotating, anticyclonic) vortex streamers on the northern and southern sides of the Kuroshio in both seasons. Submesoscale eddies with typical diameters of *O* (1–10 km) arise more evidently in winter than in summer because of the mixed-layer deepening and surface cooling that precondition baroclinic and symmetric instabilities near the surface [e.g., *Thomas and Taylor*, 2010]. In contrast, mesoscale eddies with diameters of *O* (100 km) are more prominent in summer than winter, consistent with *Sasaki et al*. [2014]. The mesoscale eddies are generally shed from the coastal topographies such as capes and islands, and spontaneously generated near the Kuroshio front, occasionally resulting in meandered paths [e.g., *Endoh and Hibiya*, 2001]. For the latter, the release of the available potential energy around the Kuroshio front leads to baroclinic instability and associated eddies [e.g., *Waseda et al*., 2003]. Such eddy generation occurs typically at a period of several days. The mesoscale eddies manifested in the KE are transported downstream along the Kuroshio at about 1–2° per day. In contrast, in the KR, quasiperiodic cyclonic-eddy shedding takes place from the upstream headland topography. These eddies eventually coalesce due to inverse cascade to evolve into the cyclonic lateral recirculation under the relatively stable Kuroshio path [e.g., *Yamagata and Umatani*, 1989; *Nishimura*, 1998]. Submesoscale eddies do not manifest on the Kuroshio path, where the SST front is prominent (Figure 2f), but rather in the region $\sim$1° away from the front. The submesoscale dominance is also found in the surface kinetic energy wave number (k) spectra as elevated power at higher wave numbers in the KR and the KE (see Figure 1b for the subdomain definitions), as shown in Figure 4. The spectral power for the KR and KE is greater at higher wave numbers in winter with gentler spectral slopes close to the k^{-3} law expected for quasi-geostrophic turbulence [e.g., *Charney*, 1971], rather than to the k^{-2} law [cf., *Capet et al*., 2008; *Sasaki et al*., 2014]. The KR shows less prominent seasonal differences, whereas interseasonal differences in the spectral energy are more evident in the KE for our choice of analysis subdomains (Figure 1b). These results demonstrate that both regions are affected by vigorous eddy activity with more energetic submesoscale eddies in winter.

The surface eddy kinetic energy, EKE $=\left(\overline{u'^2}+\overline{v'^2}\right)/2$, is then evaluated from the ROMS result (Figure 5a), where u and v are the zonal and meridional components of the horizontal velocity, the overbar is an ensemble-averaging operator, and prime denotes high-pass filtered fluctuations relative to the seasonal components for timescales longer than 90 days. High EKE is distributed along the Kuroshio, corresponding

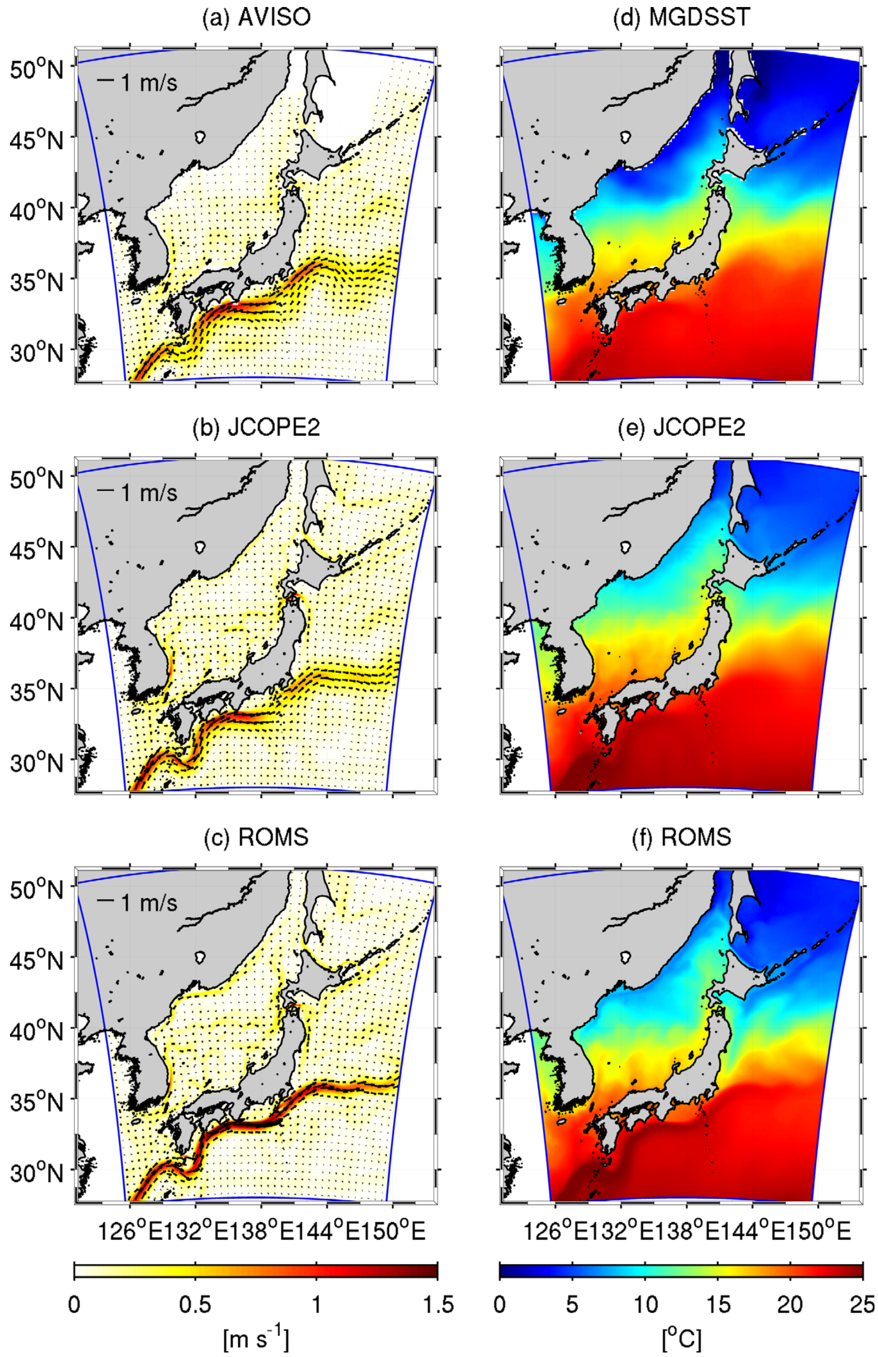

Figure 2. Plan view plots of the climatological surface velocity vectors and their magnitude in color (left column) and sea-surface temperature (SST; right column). The top panels are from the (a) AVISO and (d) MGDSST data. The middle and bottom plots depict the JCOPE2 reanalysis and the present ROMS model.

to the vorticity snapshot in Figure 3. The EKE is confined near the Kuroshio path in the KR, while it is extensively distributed in the meridional direction in the KE. In the KR, the Kuroshio path is rather persistent, although the KE jet leads to meandered paths with much greater spatiotemporal variability (not shown). Figure 5b shows the annually averaged SSH and subsampled surface current velocity vectors in the expanded subregion indicated by the magenta box in Figure 5a. The Kuroshio passes Cape Shionomisaki (CS) to take the eastward path and then veers northeastward at ~138.2°E off Cape Omaezaki (CO) and gets close to the coast again before entering the KE. At the margin between the Kuroshio and coastline, two quasi-persistent standing eddies are found: a mesoscale cyclonic eddy with lowered SSH at ~100 km off CO

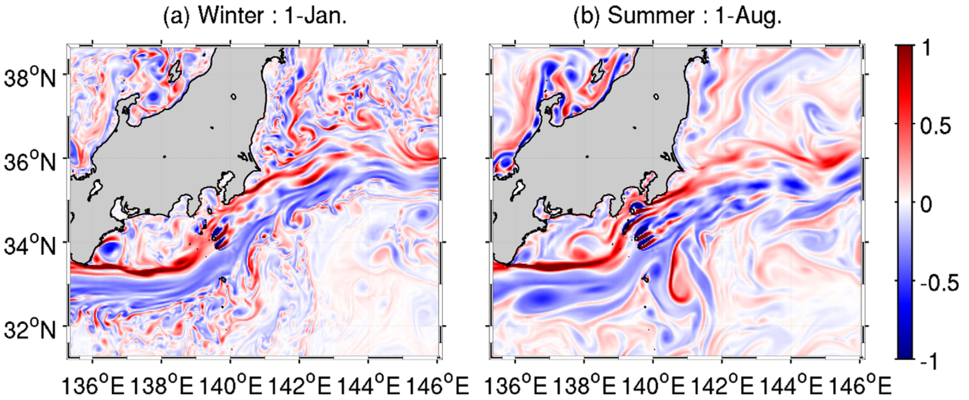

Figure 3. Instantaneous (daily averaged) surface relative vorticity normalized by the Coriolis parameter (i.e., dimensionless) on (a) 1 January (winter) and (b) 1 August (summer) in the 10th model year. A pair of positive and negative vortex streamers is apparent around the Kuroshio path with substantial changes in the eddy size. Submesoscale eddies with diameters of *O* (1–10) km are more evident in winter.

and an anticyclonic eddy with slightly elevated SSH in the east of CS. Because cyclonic eddies are accompanied by localized upwelling that promotes the nutrient supply from the nutrient-rich subsurface to the near-surface euphotic zone, the mesoscale cyclonic eddy off CO is expected to maintain the biological production in the KR, as suggested by *Kimura et al.* [1997].

3.3. Upper-Ocean Biogeochemistry

The annually averaged surface chl-a climatologies from the ROMS-NPZD model and the MODIS/Aqua satellite data are compared in Figure 6. Several basic features are consistently observed even with the simple nitrogen-based NPZD model, although the model result is not perfect. For instance, segmentation in the production occurs on the northern and southern sides of the Kuroshio, with much higher chl-a to the north. Coastal enhancement of chl-a is commonly shown, whereas the model shows an underestimation because of the lack of the land-derived nutrient inputs. In turn, chl-a is slightly overestimated in the northeastern part of the model domain, where the primary productivity is known to decrease due to iron limitation [e.g., *Denman and Abbott*, 1994; *Denman*, 2008; *Moore et al.*, 2013], which is not considered in the present model. Nevertheless, the modeled surface chl-a concentrations of 1.2–1.8 μg L^{-1} in the KR and 1.0–1.5 μg L^{-1} in the KE are also quantitatively comparable to the in situ measurements [e.g., *Kimura et al.*, 1997; *Clayton et al.*, 2014]. Therefore, we consider the simplified geophysics-biogeochemistry relationship employed here to be useful to diagnose biological responses to eddying flow fields in the upper ocean around the Kuroshio, avoiding further complexity of more sophisticated biogeochemical models. We leave these issues for future work.

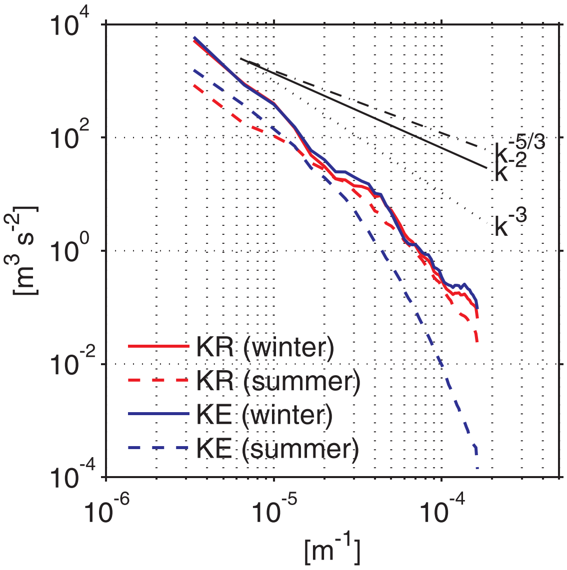

Figure 4. Surface kinetic energy wave number spectra for winter (January–March) and summer (July–September) in the KR and KE subdomains shown in Figure 1b. The spectral slopes become gentler in winter than in summer due to energetic submesoscale eddies.

The model shows that the cyclonic eddy developed in the coastal area off CO in the KR (Figure 5b) supplies subsurface nutrients to the near-surface euphotic zone, leading to active production in the coastal area north of the Kuroshio path (Figure 6b). However, chl-a is reduced along the Kuroshio path, where the EKE is considerably high (Figure 5a). In contrast, the maximum chl-a appears mostly on the mean Kuroshio path in the KE around the zonal band of the Kuroshio Extension jet at 35°N and 141–148°E (Figures 2c and 5b), where the EKE is also high (Figure 5a). These results suggest that the eddy activities associated with the Kuroshio in both regions influence the primary production differently.

To understand the meridional transition of the primary production across the Kuroshio, the vertical structures of nitrate and chl-a are examined. We choose the stations at 138°E and 145°E centered at the Kuroshio core, which is defined by the location of the maximum velocity magnitude at 50 m depth, and the stations at ±1° meridionally away from the core (Figure 1b). Figure 7 shows the Hovmöller diagrams of the modeled nitrate and chl-a at the three stations at 138°E (KR); the white lines represent the KPP-derived mixed-layer depths [*Large et al.*, 1994]. Nitrate is distributed near the surface on the north side (Figure 7a) to maintain the high production in the mixed-layer (Figure 7d). Upward nitrate transport and the associated high biological production are pronounced in colder seasons (December–March) when the mixed-layer deepens. Going southward (i.e., equatorward), nitrate is lowered, barely reaches the surface, and results in reduced chl-a. In warmer seasons, however, high chl-a is observed within and slightly below the mixed-layer, leading to nitrate depletion (Figures 7d–7f). The spring bloom with

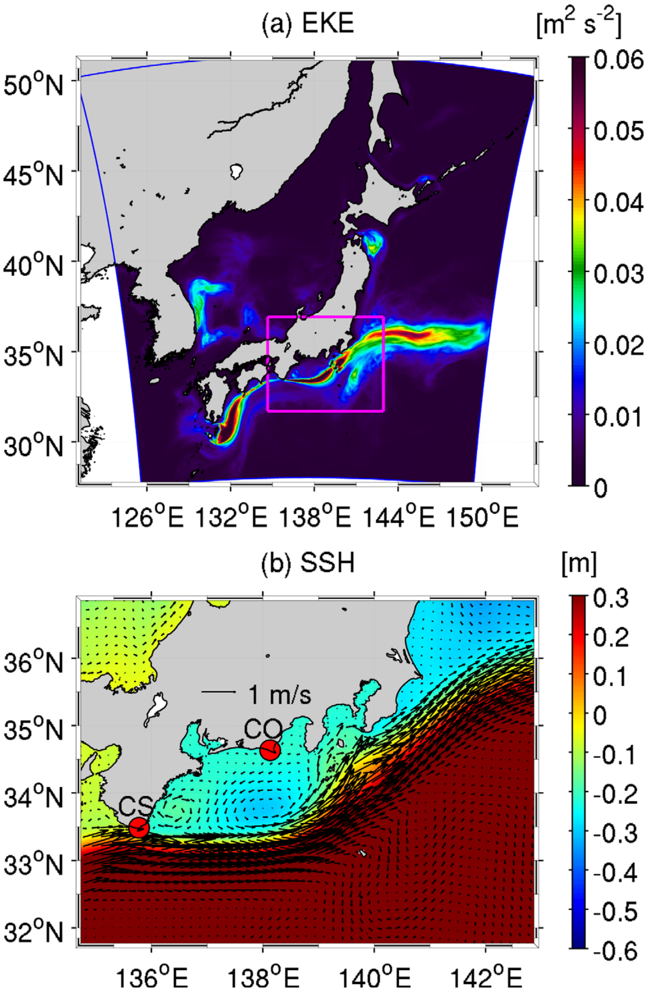

Figure 5. Plan view plots of the annually averaged (a) surface eddy kinetic energy (EKE), and (b) sea surface height (SSH) in color with the surface current velocity vectors in the blow-up region shown by the magenta box in Figure 5a. The red circles indicate Cape Omaezaki (CO) and Cape Shionomisaki (CS). The EKE is distributed mostly along the Kuroshio path. A counter-clockwise, cyclonic mesoscale eddy is formed off CO.

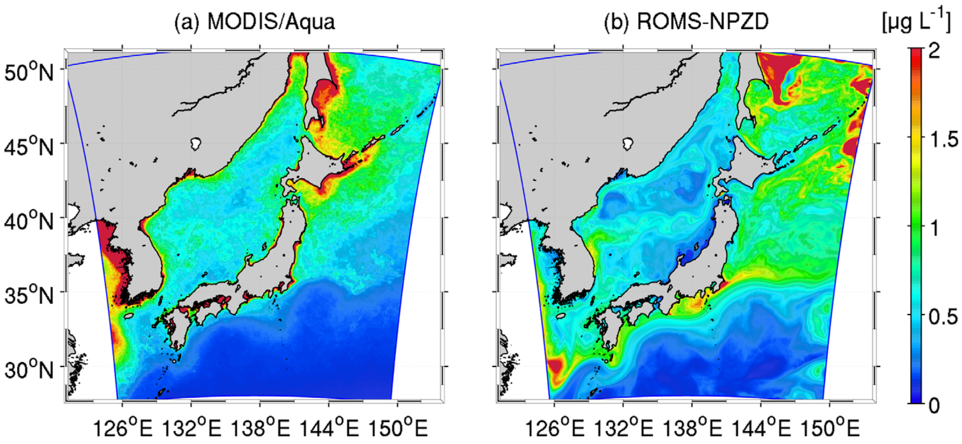

Figure 6. Surface chlorophyll-a (chl-a) concentrations from (a) the climatology of MODIS/Aqua satellite data, and (b) the annually averaged ROMS-NPZD model. The productivity is high in the north of the Kuroshio, where the cold subarctic water dominates, and coastal margins, whereas the southern chl-a is considerably reduced.

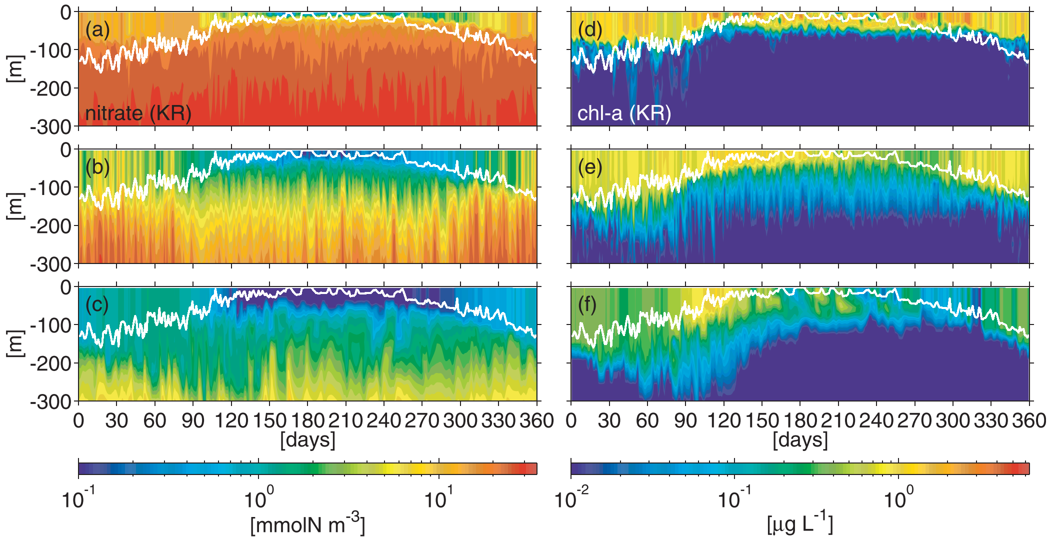

Figure 7. Hovmöller diagrams of the $\log_{10}$-based nitrate (left column) and chlorophyll-a (right column) concentrations in the (a and d) northern, (b and e) Kuroshio core, and (c and f) southern locations along the 138°E line in the Kuroshio Region (KR) as shown by the red stars in Figure 1b. The white lines are the KPP-determined mixed-layer depths. Substantial meridional transitions are apparent both in nitrate and chlorophyll-a; the northern location has a higher productivity and nutrient depletion in the upper ocean than the southern locations.

increased chl-a occurs at the two southern stations in April and May (Figures 7e and 7f). Similar seasonal variability, meridional differences in nitrate, and chl-a are observed in the KE at 145°E (Figure 8), while the upper limit of the high nitrate concentration is lowered more pronouncedly than that in the KR (Figure 7). It is worth noting that the nitrogen budget analysis (not shown) indicates that nitrogen exists mostly in the phytoplankton and zooplankton compartments in both the KR and KE during the bloom. The increased zooplankton further enriches the detritus that settles down by ~100 m, resulting in the increase of ammonium below the mixed-layer. Furthermore, both nitrate and chl-a have high frequency fluctuations at a period of several days, suggesting that the transient Kuroshio and associated eddies are responsible for generating the vertical nitrate fluxes that maintain the upper-ocean production in a different way in each of the two regions.

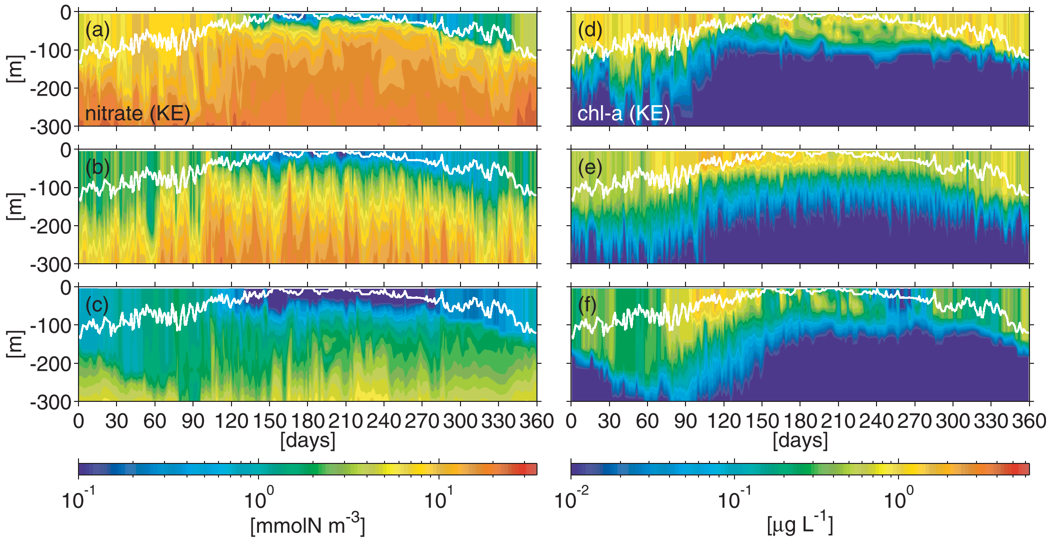

Figure 8. Same as Figure 7, but for the 145°E line in the Kuroshio Extension Region (KE; see Figure 1b). The near-surface chlorophyll-a at the southern stations (e and f) is higher than that in the Kuroshio Region (KR) in Figure 7.

Table 3. Seasonally and Annually Averaged Chlorophyll-a (chl-a) and Eddy-Induced Vertical Nitrate Flux ($\overline{N'w'}$) Integrated Vertically From the Surface Down to 50 and 200 m depths as labeled, While Averaged Spatially Over the Two Transects at 138°E (KR) and 145°E (KE), as Shown in Figure 1b[a]

Variable	Region	Depth (m)	Winter	Spring	Summer	Fall	Annual
Chl-a (μg L^{-1} m)	KR	50	34.1	41.8	29.4	27.4	33.2
		200	69.6	65.4	34.5	33.6	50.8
	KE	50	29.4	44.0	26.8	26.9	31.8
		200	79.7	80.7	36.7	39.9	59.3
	KE/KR	200	1.145	1.235	1.062	1.188	1.167
Nitrate flux (μmol N m^{-1} s^{-1})	KR	50	−1.31	−0.68	0.08	−0.02	−0.48
		200	−2.85	−1.34	0.16	−0.31	−1.08
	KE	50	0.13	0.10	0.11	0.00	0.09
		200	3.41	2.36	0.47	−0.18	1.51

[a] Note that we define the four seasons as December–February (winter), March–May (spring), June–August (summer), and September–November (fall), respectively. KE/KR denotes the ratio of the chl-a in the Kuroshio Extension Region (KE) to that in the Kuroshio Region (KR).

Surface and subsurface primary production occurs more prominently in the KE, except for the northern location, where the nitrate concentrations below the mixed-layer and the near-surface chl-a are higher in the KR due to the cyclone-induced upwelling (section 3.2). Table 3 summarizes the time-averaged primary production as the vertically integrated chl-a concentration from the surface down to $z = -50$ and -200 m, averaged laterally along the 138°E and 145°E transects (Figure 1b). Evidently, the KE is always more productive than the KR at 16.7% (annual) down to 200 m depth as indicated by the chl-a KE/KR ratio, with the seasonality ranging from 6.2% to 23.5%. Spring bloom is detected particularly in the photosynthetically active near-surface layer down to a depth of 50 m in both regions, as exhibited in Figures 7 and 8. Note that the near-surface chl-a differences between the KR and KE in Table 3 are statistically significant with $p < 0.002$ (i.e., at the 99.8% significance level) according to the two-sample t test, except for summer with $p = 0.15$.

4. Eddy-Induced Nitrate Transport

To assess the spatial distribution of nitrate influencing the upper-ocean production, the isoconcentration depths (ICDs) of the annually averaged nitrate of 20 mmol N m^{-3} from the ROMS-NPZD model are depicted in Figure 9. The ICDs are closely related to the surface chl-a distribution (Figure 6b), with apparent inverse proportionality. The shallower the ICDs are, the higher is the surface chl-a. On the Pacific side of Japan, the deeper ICDs coincide with depleted production, in particular in the south of the Kuroshio path, where subtropical warm water dominates. The ICDs almost surface in the KR, where the upwelling due to the standing cyclonic mesoscale eddy is expected to promote the upward nutrient transport. However, the southward ICD deepening occurs with a steeper slope than in the KE, where the ICDs in the north of the Kuroshio are deeper than those in the KR. The deepest ICDs emerge in the south of the Kuroshio (as deep as 600 m) in both regions, suggesting that the downward subsurface nitrate transport takes place across the Kuroshio to induce the southward downgradient of the ICDs. The ICDs of the Kuroshio core also vary seasonally (not shown); they are generally elevated in warmer seasons, as partly depicted in Figures 7 and 8.

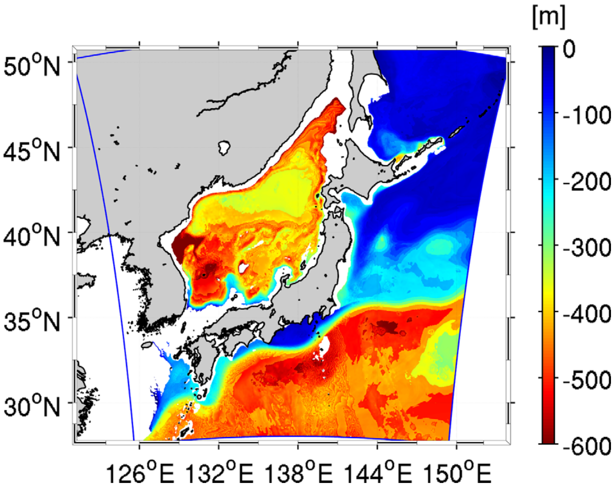

Figure 9. Annually averaged depths of the nitrate isoconcentration (ICDs) of 20 mmol N m^{-3}. Notice the shallowing in the north of the Kuroshio and southward sharp deepening in the meridional direction across the Kuroshio. The ICDs almost surface near the shore of the Kuroshio Region (KR; Figure 1b), manifesting a more intensive southward downgradient than that in the Kuroshio Extension Region (KE).

To investigate the vertical nitrate transport in both regions, cross-sectional

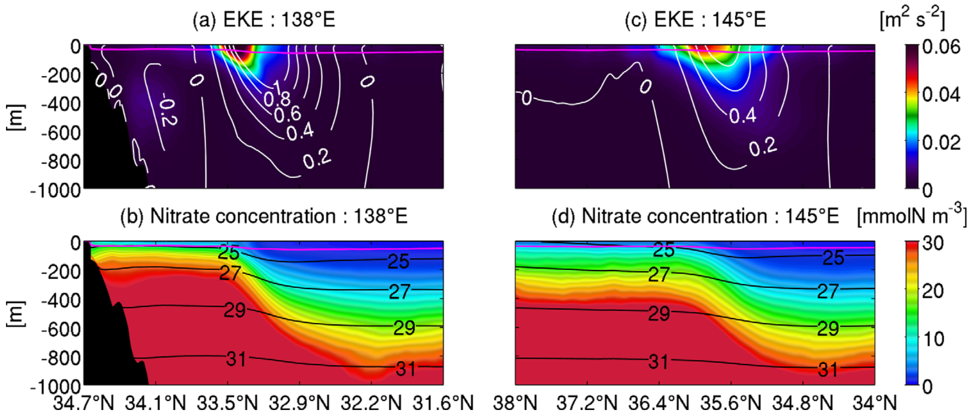

Figure 10. Cross-sectional plots of the annually averaged eddy kinetic energy (EKE; upper row) and nitrate concentration (lower row) along the 138°E transect (left column) in the Kuroshio Region (KR; Figure 1b) and the 145°E transect (right column) in the Kuroshio Extension Region (KE) in color. Also plotted by contour lines are the eastward velocities in m s^{-1} normal to the section (upper) and the potential density in kg m^{-3} (lower). The magenta lines are the annually averaged mixed-layer depth estimated by the KPP model.

distributions of the annually averaged EKE and nitrate concentrations along the two transects at 138°E and 145°E (Figure 1b) are shown in Figure 10. The eastward velocities normal to each transect and potential density overlaid as contours. The KPP-determined mixed-layer depths are also plotted. The Kuroshio main body is located near the surface at ~33°N (KR) and 35.5°N (KE), obliquely extending southward down to a depth of ~800 m, visualized by the velocity contours of 0.2 m s^{-1}. The EKE peaks slightly northward of the velocity maximum (see also Figure 5). The EKE in the KE is less energetic, whereas it has a more extensive meridional distribution than in the KR. The southward downgradient (or subduction) of the density and nitrate consequently takes place around the Kuroshio path, although the meridional transition is more intensified in the KR (138°E) with elevated nitrate ICDs and isopycnals in the north of the Kuroshio. Note that such shoreward elevations and consequent southward nitrate downgradient are not evident in the poorly resolved WOA05 data (not shown). Because the present submesoscale eddy-permitting model indicates correlations in the spatial distributions between EKE and nitrate, these results suggest that the vertical nitrate transport is potentially affected by transient dynamics characterized by eddies associated with the Kuroshio.

To examine the influence of eddies on the nitrate transport, we evaluate the eddy-induced nitrate flux. The (vertical) nitrate flux F_V may be decomposed into the mean and eddy components as:

$$F_V = \overline{Nw} \approx \underbrace{\overline{N}\,\overline{w}}_{\text{mean}} + \underbrace{\overline{N'w'}}_{\text{eddy}}, \tag{9}$$

where w is the upward vertical velocity; N is the nitrate concentration ($\left[\mathrm{NO}_3^-\right]$); and the prime denotes the fluctuating (eddy) component for the periods shorter than 90 days computed with the Butterworth frequency filter. Likewise, the eastward and northward horizontal fluxes (F_H) are determined using u and v instead of w. Figure 11 shows the annually averaged eddy-induced horizontal (meridional) and vertical nitrate fluxes vertically integrated from the surface down to $z = -200$ m. The southward and upward transport is defined as positive. The southward eddy flux is pronounced along the Kuroshio path over the large zonal extent from 126°E to 143°E, while highly positive and lowly negative patches appear in the KE further to the east. The northward flux prevails in the north of the Kuroshio along the coast with the meridionally stretched distribution between 35°N and 43°N. The vertical eddy flux is also confined near the Kuroshio path but in a more complicated manner with manifesting sign changes as the Kuroshio flows eastward. Although negative, downward flux is prominent in the KR, the KE is dominated by weak but upward flux, consistent with the elevated nitrate distribution in Figure 10. These spatial patterns of the eddy fluxes explain the surface chl-a distribution reasonably well (Figure 6b). In the coastal area north of the KR, there are also weak upward fluxes, which correspond to the standing cyclonic eddy-induced upwelling (Figure 5b) and to the resultant high chl-a. In the north of the KE, where the cold subarctic water prevails, the intensive upward flux associated with prevailing cyclonic eddy (Figure 3) is attributed to the high production. On

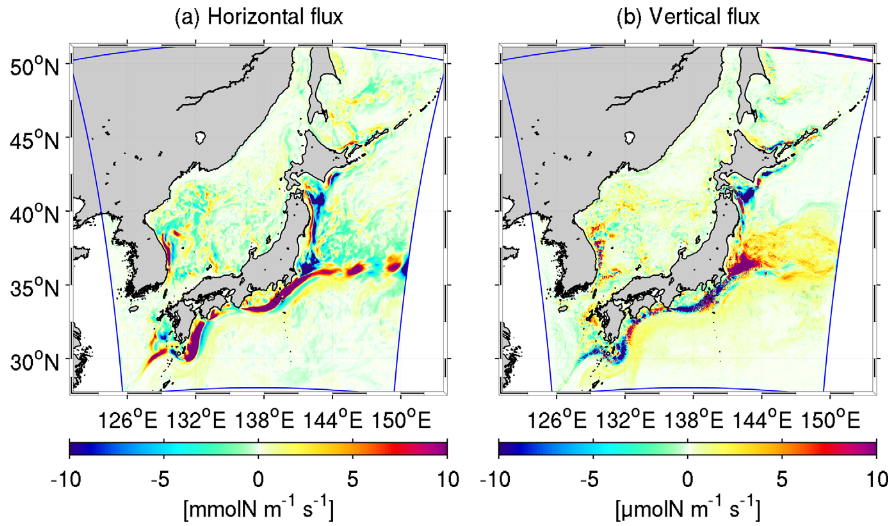

Figure 11. Annually averaged (a) horizontal and (b) vertical components of the eddy-induced nitrate flux (equation (9)), integrated vertically from the surface down to 200 m depth. The southward and upward directions are defined as positive. The eddy fluxes are distributed mostly near the Kuroshio path with prominent spatial differences in the Kuroshio Region (KR) and Kuroshio Extension Region (KE).

the contrary, chl-a in the south of the Kuroshio, where the warm subtropical water prevails, is reduced remarkably owing to the southward and downward eddy fluxes.

The subsurface eddy fluxes for the two transects along 138°E (KR) and 145°E (KE) illustrate significant structural differences (Figure 12). The southward and downward eddy fluxes in the KR are distributed around 33.5°N, where the Kuroshio main body exists (Figure 10a) within and below the mixed-layer. Because this downward flux does not occur along the isopycnals (Figure 10b), eddy mixing and associated strong turbulence are anticipated to promote this diapycnal transport. By contrast, the fluxes in the KE emerge at depths deeper than ~400 m. Thus, in the KR, a substantial amount of nitrate is removed from the near-surface euphotic zone on the coastal side and is transported downward beneath the Kuroshio by eddies, leading to the intensified nitrate reduction. In other words, the vigorous downward eddy transport competes against the cyclone-induced upwelling in the coastal part of the KR. In the KE, however, the downward eddy flux takes place at depths greater than 400 m, while the moderate upward eddy flux dominates in the upper layer (Figure 12c). This substantial difference in the vertical eddy nitrate fluxes is also evident in Table 3. In general, the KR is dominated by negative, downward fluxes except for summer, whereas the KE mainly has positive, upward fluxes. As a consequence, the eddy-induced downward nitrate transport is

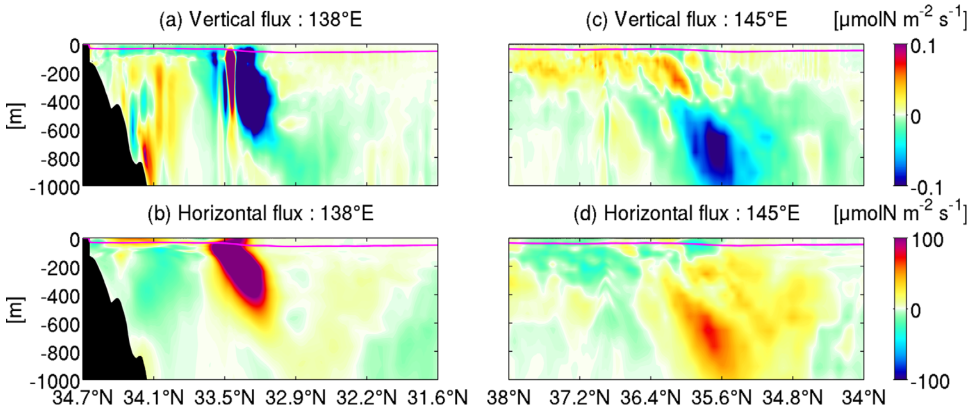

Figure 12. Cross-sectional plots of the annually averaged, horizontal (top row) and vertical (bottom row) components of the eddy-induced nitrate fluxes (equation (9)) along the 138°E (left column) and 145°E (right column) transects. The southward and upward directions are defined as positive. The magenta lines are the associated KPP-evaluated mixed-layer depth. Notice that the near-surface intensification occurs in the KR (138°E) while the subsurface, weaker fluxes are found in the KE (145°E).

anticipated to restrict the primary production around the Kuroshio path more extensively in the KR than in the KE.

Note that *Nagai et al*. [2012] reported based on a detailed measurement that shallow warm tongues and deep cold tongues were formed at the Kuroshio front in the KE due to isopycnal subduction and diapycnal turbulent mixing. The latter tongues are structurally quite similar to the deep downward eddy flux found in the KE in the present study. It is also worth noting that the vertical mean nitrate flux ($\overline{N}\overline{w}$) is insignificant as it is approximately an order of magnitude smaller than the vertical eddy flux ($\overline{N'w'}$). In addition, because the difference in the vertical eddy flux results mostly from the difference in the vertical velocity variances rather than the nitrate variances (not shown), mesoscale and submesoscale eddies associated with the transient Kuroshio have an inevitable importance for the intensified nitrate downward transport in the KR. As shown in Table 3, these vertical eddy fluxes vary seasonally to promote the nitrate seasonal variability in the upper ocean (Figures 7 and 8) caused by the seasonal variability of the eddy field, where submesoscale mixing is significantly enhanced in colder seasons, while mesoscale mixing is predominant in warmer seasons (Figures 3 and 4).

5. Eddy Generation Mechanisms

The eddy generation mechanism is examined using the energy conversion rates in an EKE conservation equation useful for quantifying the relative importance of the instability and eddy-mean interactions [e.g., *Marchesiello et al*., 2003; *Dong et al*., 2006; *Klein et al*., 2008]. We investigate the two important quantities, the barotropic and baroclinic conversion rates, K_mK_e and P_eK_e, respectively, defined as follows:

$$K_mK_e=-\left(\overline{u'u'}\,\frac{\partial\overline{u}}{\partial x}+\overline{u'v'}\,\frac{\partial\overline{u}}{\partial y}+\overline{u'w'}\,\frac{\partial\overline{u}}{\partial z}+\overline{v'u'}\,\frac{\partial\overline{v}}{\partial x}+\overline{v'v'}\,\frac{\partial\overline{v}}{\partial y}+\overline{v'w'}\,\frac{\partial\overline{v}}{\partial z}\right), \tag{10}$$

$$P_eK_e=-\frac{g}{\rho_0}\overline{\rho'w'}, \tag{11}$$

where x, y, and z are the horizontal and vertical coordinates; ρ is the density of the sea water; $\rho_0=1027.5$ kg m^{-3} is the reference density; and g is the gravitational acceleration. Note that K_mK_e represents the conversion of the mean kinetic energy to EKE by horizontal and vertical Reynolds stresses due to shear instability if $K_mK_e>0$. In contrast, P_eK_e represents the eddy available potential energy converted to EKE by baroclinic instability if $P_eK_e>0$. When K_mK_e and P_eK_e are negative, EKE is decreased and leads to flow stabilization, merging of eddies, or restratification.

The annually averaged conversion rates are plotted as the horizontal distributions, integrated vertically from the surface down to $z=-200$ m (Figure 13), and as the cross-sectional distributions along the 138°E (KR) and 145°E (KE) transects (Figure 14). Figure 15 shows the meridional profiles of the vertically integrated, eddy-induced horizontal (southward) and vertical (upward) nitrate fluxes (F_H and F_V), K_mK_e, and P_eK_e along the two transects. In Figure 13, both conversion rates are mostly distributed near the Kuroshio path, where EKE is high (Figure 5), with distinctive meridional sign changes in K_mK_e. A positive K_mK_e is manifested on the northern (southern) side of the Kuroshio path in the KR (KE). Inflection point instability associated with zonal free jets should have a positive K_mK_e on both sides of the velocity maximum, as seen in the K_mK_e distribution around the KR, while the topographic eddy shedding overrides in many places along the Kuroshio including the KE. A positive P_eK_e is generally provoked along the path, except for a few places including the Izu Ridge (at ~34.23°N and 139.25°E). Figure 13 shows that the positive K_mK_e developed in the south of the Kuroshio originates from the Izu Ridge, where P_eK_e changes its sign to negative and subsequently extends to the KE and further to the east. In turn, P_eK_e is positive in the KR and the west of the KE, while it almost vanishes in the KE. Similarly, the headland topography around Cape Shionomisaki (viz., CS; Figure 5b) has a positive K_mK_e on the northern side of the Kuroshio in the KR. These results show that the ridge and headland topographies have a considerable impact on the altering roles that eddies play and yield some residual effects on their downstream areas.

Near the surface, the maximum velocity (Figure 10) appears at ~33.1°N (KR) and 35.8°N (KE); however, Figures 14 and 15 indicate that the maximum positive K_mK_e occurs at ~33.5°N (KR) and 35.4°N (KE). In the KR, the near-surface EKE peak (Figure 10) collocates with the maximum K_mK_e, where P_eK_e also significantly

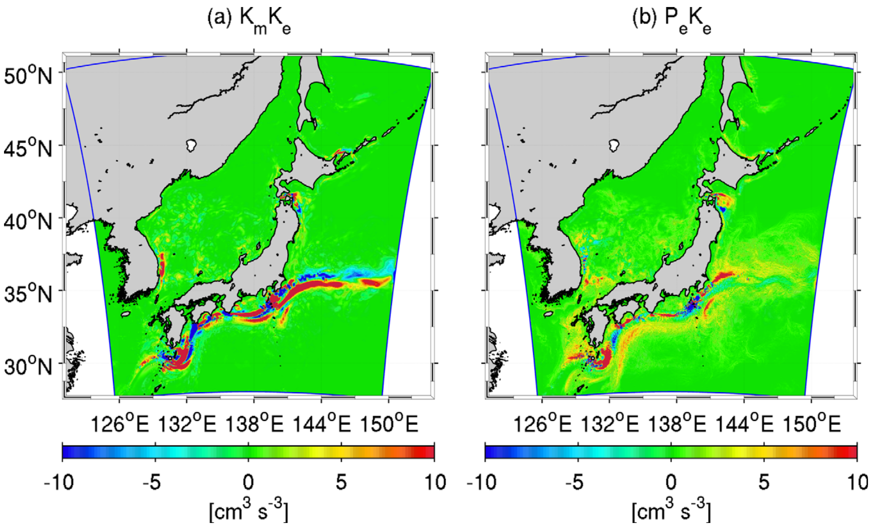

Figure 13. Annually averaged (a) barotropic conversion rate K_mK_e and (b) baroclinic conversion rate P_eK_e (equations (10) and (11)) integrated vertically from the surface down to 200 m depth. Both K_mK_e and P_eK_e are provoked around the Kuroshio path with pronounced sign changes in the streamwise and meridional directions.

increases its magnitude. The K_mK_e and P_eK_e maxima are observed where the nitrate isoconcentration deepens southward due to the eddy-driven nitrate downward transport in the KR (Figures 9, 10b, and 12a). This deepening is further amplified by the near-surface F_V (Figure 15a), which changes its direction from upward on the northern side of the Kuroshio to downward on the other side. The former is coincident with the intensified positive K_mK_e, while the latter occurs at the positive P_eK_e peak (Figure 15b). However, in the KE, the peaks of the near-surface EKE and K_mK_e are not coincident and remarkably small P_eK_e values appear (Figures 14c–14d and 15d), while all of them are intensified near the mixed-layer. Both the K_mK_e and P_eK_e are attenuated when going deeper and marginally contribute to the subsurface eddy nitrate fluxes centered at ~500 m depth (Figure 12), where nitrate is abundant (Figure 10). In contrast, the maximum positive K_mK_e at 35.4°N occurs near the surface in the KE, where nitrate is considerably depleted, resulting in quite small eddy fluxes (Figure 15c). In the extensive area in the north of the KE between 38°N and the Kuroshio front at 35.6°N, a weak but positive P_eK_e is provoked (Figure 15d) to promote baroclinic instability that leads to the cyclonic eddy-induced nutrient upwelling (Figure 15c).

In summary, the large, positive K_mK_e induced from CS and the positive P_eK_e associated with the sharp front in the KR (Figure 2f) jointly enhance shear instability and baroclinic frontal instability in the upper ocean that promote eddying flows on the north side of the Kuroshio, leading to an extensive diapycnal southward

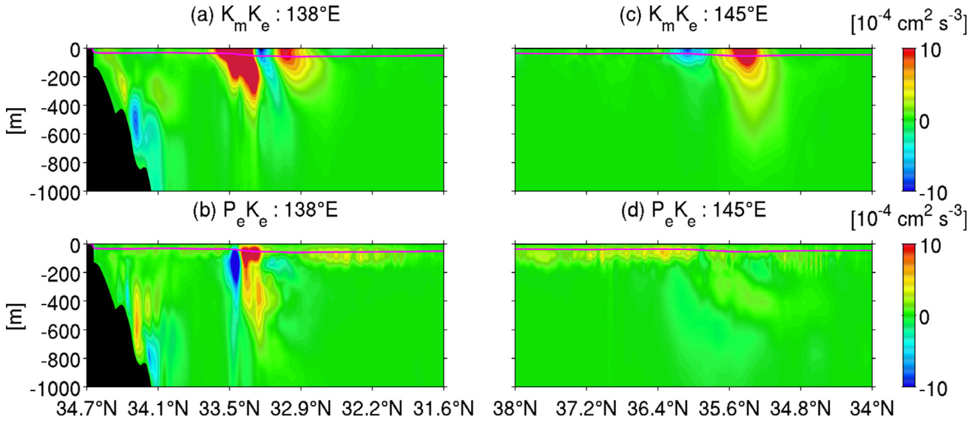

Figure 14. Cross-sectional plots of the annually averaged, barotropic conversion rate K_mK_e (top row) and baroclinic conversion rate P_eK_e (bottom row) along the 138°E (left column) and 145°E (right column) transects. The magenta lines are the associated KPP-evaluated mixed-layer depth. Shear and baroclinic instabilities jointly promote near-surface eddy-driven downward transport at around the area with higher eddy kinetic energy (EKE; Figure 10a) in the KR (138°E), although both of them are insignificant in the KE (145°E).

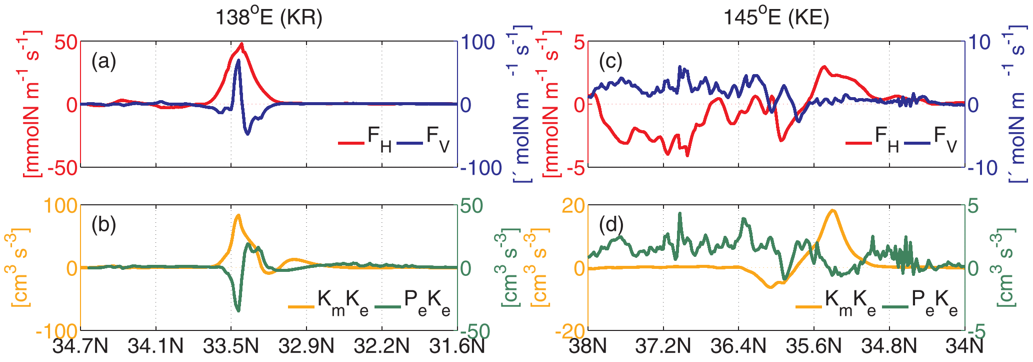

Figure 15. Meridional profiles of the eddy-induced nitrate fluxes (red: horizontal flux F_H; blue: vertical flux, F_V), barotropic conversion rate K_mK_e (yellow), and baroclinic conversion rate P_eK_e (green) along the 138°E (left column) and 145°E (right column) transects. All variables are vertically integrated from the surface down to 200 m depth. Notice different scales are used for the *y* axes in each plot. Along 138°E (KR), the downward eddy flux is induced by baroclinic instability ($P_eK_e \gg 0$) at the Kuroshio front, while the upwelling occurs mostly through shear instability ($K_mK_e \gg 0$) in the north of the downward flux. However, the near-surface downward flux is not evident along 145°E (KE) with a weak upward flux in the north of the Kuroshio.

and downward nutrient transport. In the KE, particularly east of 143°E, the negative K_mK_e provoked remotely from the Izu Ridge in conjunction with the attenuated P_eK_e in the upper ocean hinder the downward reduction of the nutrient-rich near-surface water, while subsurface southward and downward nitrate eddy transport occurs in the south of the Kuroshio path.

6. Conclusions

We examined the influences of mesoscale and submesoscale eddies associated with the transient Kuroshio on the primary productivity in the Kuroshio Region (KR) and Kuroshio Extension Region (KE) off Japan using a climatological oceanic modeling based on ROMS coupled with a simple pelagic NPZD biogeochemical model. A model-data comparison was conducted to demonstrate that the present ROMS-NPZD model reproduces the mean upper-ocean dynamics and biological responses around the Kuroshio fairly well.

The model results indicate that the surface chlorophyll-a (chl-a) distribution is closely related to the eddy activities. In general, chl-a is higher on the north side of the Kuroshio due to upwelling-favorable cyclonic eddies and resultant upward eddy nitrate flux. In particular, the standing cyclonic eddy developed between the Kuroshio and the coastline in the KR helps to maintain abundant primary production. In contrast, we observed, for the first time in the area, that the productivity on the south side of the Kuroshio is considerably limited by the southward and downward eddy-driven nitrate transport and resultant deepening of the nitrate-rich water. The eddy-induced southward lateral nitrate transport appears almost everywhere along the Kuroshio path and enhances the meridional transition. Although the higher EKE is produced around the Kuroshio path both in the KR and KE, the associated eddy activities affect the primary production in quite different ways. In the KR, the diapycnal, downward eddy nitrate flux is pronounced near the surface along the Kuroshio path to compensate the cyclone-induced upward nitrate transport. The energy conversion analysis revealed that the topographically generated positive K_mK_e (barotropic conversation rate) and frontally intensified positive P_eK_e (baroclinic conversion rate) concurrently promote the eddy-driven downward nitrate transport through shear instability and baroclinic instability, which suppress the biological production near the Kuroshio path. However, in the KE, the negative K_mK_e originated from the upstream ridge topography and weak P_eK_e give rise to upward eddy nitrate flux in the upper ocean, leading to the maintenance of the primary productivity around the Kuroshio path. The eddy-induced downward nitrate transport occurs at depths greater than 400 m on the south side of the Kuroshio in the KE. Overall, the headland and ridge topographies are found to be crucial for the changing roles of eddies in nutrient transport, which are responsible for the upper-ocean primary production through the alternation of K_mK_e and P_eK_e. As a result, the primary production is generally higher in the KE by ~23.5% (at 16.7% as the annual average) than that in the KR.

Acknowledgments
The authors appreciate the financial support from the JST-CREST program (Grant Number JPMJCR12A6). Y. Uchiyama is also grateful for the support from the JSPS grant-in-aid for Scientific Research (15H00977, 15H04049, and 15KK0207) at Kobe University. The ROMS-NPZD model is available from A. F. Shchepetkin upon request (alex@atmos.ucla.edu). The JCOPE2 reanalysis data set is freely available for scientific purposes upon request to APL/JAMSTEC (jcope@jamstec.go.jp). The STRM30_Plus data are available at ftp://topex.ucsd.edu/pub/srtm30_plus/. The J-EGG500 data set is distributed by JODC at http://jdoss1.jodc.go.jp/cgi-bin/1997/depth500_file. The MSLA (mapped sea-level anomaly) in delayed-time product was generated by Ssalto/Duacs and distributed by AVISO (ftp.aviso.altimetry.fr). The GPV-GSM atmospheric product was generated by JMA and is available from the repository at http://database.rish.kyoto-u.ac.jp/arch/jmadata/data/gpv/original/. The COADS and WOA05 data are maintained and distributed by NOAA at https://www.esrl.noaa.gov/psd/data/gridded/data.coads.1deg.html and https://www.nodc.noaa.gov/OC5/WOA05/pr_woa05.html. The gridded MODIS/Aqua satellite surface chl-a product is available at https://oceandata.sci.gsfc.nasa.gov/MODIS-Aqua/Mapped. The MGDSST data set is generated and distributed by JMA at http://ds.data.jma.go.jp/gmd/goos/data/rrtdb/file_list.php.

References

Becker, J. J., et al. (2009), Global bathymetry and elevation data at 30 arc seconds resolution: SRTM30_PLUS, *Mar. Geod.*, *32*(4), 355–371.

Behrenfeld, M. J., and P. G. Falkowski (1997), Photosynthetic rates derived from satellite-based chlorophyll concentration, *Limnol. Oceanogr.*, *42*(1), 1–20.

Bracco, A., S. Clayton, and C. Pasquero (2009), Horizontal advection, diffusion, and plankton spectra at the sea surface, *J. Geophys. Res.*, *114*, C02001, doi:10.1029/2007JC004671.

Capet, X., J. C. McWilliams, J. M. Molemaker, and A. F. Shchepetkin (2008), Mesoscale to submesoscale transition in the California current system. Part I: Flow structure, eddy flux, and observational tests, *J. Phys. Oceanogr.*, *38*, 29–43.

Charney, J. (1971), Geostrophic turbulence, *J. Atmos. Sci.*, *28*, 1087–1095.

Clayton, S., T. Nagai, and M. J. Follows (2014), Fine scale phytoplankton community structure across the Kuroshio Front, *J. Plankton Res.*, *36*, 1017–1030.

Crawford, W. R., P. J. Brickley, and A. C. Thomas (2007), Mesoscale eddies dominate surface phytoplankton in the northern Gulf of Alaska, *Prog. Oceanogr.*, *75*, 287–303.

Denman, K. L. (2008), Climate change, ocean processes and ocean iron fertilization, *Mar. Ecol. Prog. Ser.*, *364*, 219–225, doi:10.3354/meps07542.

Denman, K. L., and M. R. Abbott (1994), Time scales of pattern evolution from cross-spectrum analysis of advanced very high resolution radiometer and coastal zone color scanner imagery, *J. Geophys. Res.*, *99*, 7433–7442.

Di Lorenzo E., A. J. Miller, D. J. Neilson, B. D. Cornuelle, and J. R. Moisan (2004), Modelling observed California Current mesoscale eddies and the ecosystem response, *Int. J. Remote Sens.*, *25*, 7–8, 1307–1312, doi:10.1080/01431160310001592229.

Dong, C., J. C. McWilliams, and A. F. Shchepetkin (2006), Island Wakes in Deep Water, *J. Phys. Oceanogr.*, *37*, 962–981.

Endoh, T., and T. Hibiya (2001), Numerical simulation of the transient response of the Kuroshio leading to the large meander formation south of Japan, *J. Geophys. Res.*, *106*, 26,833–26,850.

Falkowski, P. G., D. Ziemmann, Z. Kolber, and P. K. Bienfang (1991), Role of eddy pumping in enhancing primary production in the ocean, *Nature*, *352*, 55–58.

Fasham, M. J. R., H. W. Ducklow, and S. M. McKelvie (1990), A nitrogen-based model of plankton dynamics in the oceanic mixed layer, *J. Mar. Res.*, *48*, 591–639.

Franks, P. J. S., and L. J. Walstad (1997), Phytoplankton patches at fronts: A model of formation and response to wind events, *J. Mar. Res.*, *55*, 1–29.

Garcia, H. E., R. A. Locarnini, T. P. Boyer, and J. I. Antonov (2006), World Ocean Atlas 2005, in *Nutrients (Phosphate, Nitrate, and Silicate)*, vol. 4, edited by S. Levitus, *NOAA Atlas NESDIS 64*, 396 pp., U.S. Gov. Print. Off., Washington, D. C.

Gower, J. F. R., K. L. Denman, and R. L. Holyer (1980), Phytoplankton patchiness indicates the fluctuations spectrum of mesoscale oceanic structure, *Nature*, *288*, 157–159.

Gruber, N., H. Frenzel, S. C. Doney, P. Marchesiello, J. C. McWilliams, J. R. Moisan, J. J. Oram, G.-K. Plattner, and K. D. Stolzenbach (2006), Eddy-resolving simulation of plankton ecosystem dynamics in the California Current System, *Deep-Sea Res., Part I*, *539*, 1483–1516.

Gruber, N., Z. Lachkar, H. Frenzel, P. Marchesiello, M. Münnich, J. C. McWilliams, T. Nagai, and G.-K. Plattner (2011), Eddy-induced reduction of biological production in eastern boundary upwelling systems, *Nat. Geosci.*, *4*, 787–792.

Kimura, S., A. Kasai, H. Nakata, T. Sugimoto, J. H. Simpson, and J. V. S. Cheok (1997), Biological productivity of meso-scale eddies caused by frontal disturbances in the Kuroshio, *ICES J. Mar. Sci.*, *54*, 179–192.

Klein, P., B.-L. Hua, G. Lapeyre, X. Capet, S. Le Gentil, and H. Sasaki (2008), Upper ocean turbulence from high-resolution 3D simulations, *J. Phys. Oceanogr.*, *38*, 1748–1763.

Large, W. G., J. C. McWilliams, and S. C. Doney (1994), Oceanic vertical mixing: A review and model with a nonlocal boundary layer parameterization, *Rev. Geophys.*, *32*, 363–403.

Lévy, M. (2003), Mesoscale variability of phytoplankton and of new production: Impact of the large-scale nutrient distribution, *J. Geophys. Res.*, *108*(C11), 3358, doi:10.1029/2002JC001577.

Lévy, M., P. Klein, and A.-M. Treguier (2001), Impact of sub-mesoscale physics on production and subduction of phytoplankton in an oligotrophic regime, *J. Mar. Res.*, *59*, 535–565.

Marchesiello, P., J. C. McWilliams, and A. Shchepetkin (2003), Equilibrium structure and dynamics of the California current system, *J. Phys. Oceanogr.*, *33*, 753–783.

Martin, J. H., G. A. Knauer, D. M. Karl, and W. W. Broenkow (1987), VERTEX: Carbon cycling in the northeastern Pacific, *Deep-Sea Res., Part I*, *34*, 267–285.

Mason, E., J. Molemaker, A. F. Shchepetkin, F. Colas, J. C. McWilliams, and P. Sangrà (2010), Procedures for offline grid nesting in regional ocean models, *Ocean Modell.*, *35*, 1–15.

Masumoto, Y., et al. (2004), A fifty-year-eddy-resolving simulation of the world ocean: Preliminary outcomes of OFES (OGCM for the Earth Simulator), *J. Earth Simul.*, *1*, 35–56.

Matsuno, T., J.-S. Lee, and S. Yanao (2009), The Kuroshio exchange with the South and East China Seas, *Ocean Sci.*, *5*, 303–312.

Miyazawa, Y., R. Zhang, X. Guo, H. Tamura, D. Ambe, J. Lee, A. Okuno, H. Yoshinari, T. Setou, and K. Komatsu (2009), Water mass variability in the Western North Pacific detected in 15-year eddy resolving ocean reanalysis, *J. Oceanogr.*, *65*, 737–756.

Moisan, J. R., and E. E. Hofmann (1996), Modeling nutrient and plankton processes in the California coastal transition zone: 1: A time- and depth-dependent model, *J. Geophys. Res.*, *101*, 22,647–22,676.

Moore, C. W., et al. (2013), Processes and patterns of oceanic nutrient limitation, *Nat. Geosci.*, *6*, 701–710.

Morel, A., and J.-F. Berthon (1989), Surface pigments, algal biomass profiles and potential production of the euphotic layer: Relationships reinvestigated in view of remote sensing applications, *Limnol. Oceanogr.*, *34*, 1545–1562.

Nagai, T., A. Tandon, H. Yamazaki, M. J. Doubell, and S. Gallager (2012), Direct observations of microscale turbulence and thermohaline structure in the Kuroshio Front, *J. Geophys. Res.*, *117*, C08013, doi:10.1029/2011JC007228.

Nakata, H., S. Kimura, Y. Okazaki, and A. Kasai (2000), Implications of meso-scale eddies caused by frontal disturbances of the Kuroshio current for anchovy recruitment, *J. Mar. Sci.*, *57*, 143–152.

Nellemann, C., E. Corcoran, C. M. Duarte, L. Valdés, C. De Young, L. Fonseca, and G. Grimsditch (Eds.) (2009), *Blue Carbon. A Rapid Response Assessment*, 78 pp., U.N. Environ. Program., GRID-Arendal, Birkeland Trykkeri AS, Norway.

Nishimura, T. (1998), The coherent structure inside the oceanic turbulence around Japan-islands-chain, *Tech. Rep., Sci. Univ. of Tokyo*, 103 p., Noda, Japan.

Oschlies, A. (2001), Model-derived estimates of new production: New results point towards lower values, *Deep Sea Res., Part II*, *48*, 2173–2197.

Oschlies, A. (2002), Can eddies make ocean deserts bloom?, *Global Biogeochem. Cycles*, *16*, 1106–1116.

Oschlies, A., and V. Garçon (1998), Eddy-induced enhancement of primary production in a model of the North Atlantic Ocean, *Nature*, *394*, 266–269.

Pasquero, C. (2005), Differential eddy diffusion of biogeochemical tracers, *Geophys. Res. Lett.*, *32*, L17603, doi:10.1029/2005GL023662.

Roads, J. (2004), Experimental Weekly to Seasonal U.S. Forecasts with the Regional Spectral Model, *Bull. Am. Meteorol. Soc.*, *85*, 1887–1902.

Rodriguez, E., C. S. Morris, J. E. Belz, E. C. Chapin, J. M. Martin, W. Daffer, and S. Hensley (2005), An Assessment of the SRTM Topographic Products, *Tech. Rep. JPL DO31639*, 143 pp., Jet Propul. Lab., Pasadena, Calif.

Sakurai, T., Y. Kurihara, and T. Kuragano (2005), Merged satellite and in-situ data global daily SST, in *Proceedings of the International Geoscience and Remote Sensing Symposium*, *Seoul, South Korea*, pp. 2606–2608, Inst. Electr. Electron. Eng., New York.

Sasai, Y., H. Sasaki, K. Sasaoka, A. Ishida, and Y. Yamanaka (2007), Marine ecosystem simulation in the eastern tropical Pacific with a global eddy resolving coupled physical-biological model, *Geophys. Res. Lett.*, *34*, L23601, doi:10.1029/2007GL031507.

Sasai, Y., K. J. Richards, A. Ishida, and H. Sasaki (2010), Effects of cyclonic mesoscale eddies on the marine ecosystem in the Kuroshio Extension region using an eddy-resolving coupled physical-biological model, *Ocean Dyn.*, *60*, 693–704.

Sasaki, H., P. Klein, B. Qiu, and Y. Sasai (2014), Impact of oceanic-scale interactions on the seasonal modulation of ocean dynamics by the atmosphere, *Nature Comm.*, *5*, 5636, doi:10.1038/ncomms6636.

Spall, M. A. (1995), Frontogenesis, subduction and cross-front exchange at upper ocean fronts, *J. Geophys. Res.*, *100*, 2543–2557.

Spall, S. A., and K. J. Richards (2000), A numerical model of mesoscale frontal instabilities and plankton dynamics-I. Model formulation and initial experiments, *Deep-Sea Res., Part I*, *47*, 1261–1301.

Shchepetkin, A. F., and J. C. McWilliams (2005), The regional ocean modeling system (ROMS): A split-explicit, free-surface, topography-following-coordinate oceanic model, *Ocean Modell.*, *9*, 347–404.

Shchepetkin, A. F., and J. C. McWilliams (2008), Computational kernel algorithms for fine-scale, multiprocess, longtime oceanic simulations, in *Handbook of Numerical Analysis: Computational Methods for the Ocean and the Atmosphere*, pp. 119–181, edited by R. Temam and J. Tribbia, Elsevier, Amsterdam.

Strass, V. H. (1992), Chlorophyll patchiness caused by mesoscale upwelling at fronts, *Deep-Sea Res., Part A*, *39* (1), 75–96.

Teira, E., B. Mouriño, E. Marañón, V. Pérez, M. J. Pazó, P. Serret, D. de Armas, J. Escánez, E. M. S. Woodward, and E. Fernández (2005), Variability of chlorophyll and primary production in the Eastern North Atlantic Subtropical Gyre: Potential factors affecting phytoplankton activity, *Deep-Sea Res., Part I*, *52*, 569–588.

Thomas, L. N., and J. R. Taylor (2010), Reduction of the usable wind-work on the general circulation by forced symmetric instability, *Geophys. Res. Lett.*, *37*, L18606, doi10.1029/2010GL044680.

Traon, P. Y. L., F. Nadal, and N. Ducet (1998), An improved mapping method of multisatellite altimeter data, *J. Atmos. Oceanic Technol.*, *15*, 522–534.

Waseda, T., H. Mitsudera, B. Taguchi, and Y. Yoshikawa (2003), On the eddy-Kuroshio interaction: Meander formation process, *J. Geophys. Res.*, *108*(C7), 3220, doi:10.1029/2002JC001583.

Woodruff, S. D., R. J. Slutz, R. L. Jenne, and P. M. Steurer (1987), A comprehensive ocean-atmosphere data set, *Bull. Am. Meteorol. Soc.*, *68*, 1239–1250.

Yamagata, T. and S. Umatani (1989), Geometry-forced coherent structures as a model of the Kuroshio large meander, *J. Phys. Oceanogr.*, *19*, 130–138.